# GSFusion:Globally Optimized LiDAR-Inertial-Visual Mapping for Gaussian Splatting

Jaeseok Park<sup>1,2</sup>, Chanoh Park<sup>1</sup>, Minsu Kim<sup>2</sup> and Soohwan Kim<sup>2,\*</sup>

Abstract—While 3D Gaussian Splatting (3DGS) has revolutionized photorealistic mapping, conventional approaches based on camera sensor, even RGB-D, suffer from fundamental limitations such as high computational load, failure in environments with poor texture or illumination, and short operational ranges. LiDAR emerges as a robust alternative, but its integration with 3DGS introduces new challenges, such as the need for exceptional global alignment for photorealistic quality and prolonged optimization times caused by sparse data. To address these challenges, we propose GSFusion, an online LiDAR-Inertial-Visual mapping system that ensures high-precision map consistency through a surfel-to-surfel constraint in the global pose-graph optimization. To handle sparse data, our system employs a pixel-aware Gaussian initialization strategy for efficient representation and a bounded sigmoid constraint to prevent uncontrolled Gaussian growth. Experiments on public and our datasets demonstrate our system outperforms existing 3DGS SLAM systems in terms of rendering quality and mapbuilding efficiency.

#### I. INTRODUCTION

The recent advent of 3D Gaussian Splatting (3DGS) [1] has unlocked new possibilities for generating high-fidelity, photorealistic maps for autonomous robots in Simultaneous Localization and Mapping (SLAM). However, early efforts to integrate 3DGS into SLAM have predominantly relied on cameras, which require a vast number of views to build dense maps, posing a significant bottleneck for real-time performance. More fundamentally, these visionbased methods are inherently susceptible to challenging conditions such as poorly-textured regions (e.g., white walls) and varying illumination, which can lead to catastrophic failures in tracking and mapping. While RGB-D cameras were introduced to mitigate the demand for numerous views, they still rely on visual information and thus share the same vulnerabilities. Furthermore, they introduce their own distinct limitations, including a short operational range and an inability to function reliably in outdoor environments with strong sunlight.

To overcome these constraints, the SLAM community is increasingly turning to LiDAR sensors, which can robustly

This work was carried out with the support of RovifyLab, conducted by the Research Grant of Kwangwoon University in 2025, and supported by the MSIT(Ministry of Science and ICT), Korea, under the ITRC(Information Technology Research Center) support program (IITP-2025-RS-2024-00437102) supervised by the IITP(Institute for Information & Communications Technology Planning & Evaluation).

\*corresponding author.

capture precise 3D points over long distances (hundreds of meters) in real time. The integration of LiDAR has shown the potential to dramatically reduce reconstruction times from hours to mere seconds, expanding the applicability of 3DGS from indoor scenes to large-scale outdoor environments.

However, simply combining LiDAR and 3DGS creates a new set of technical challenges. First, many existing LiDAR based SLAM methods do not prioritize loop closure for global consistency. Photorealistic rendering is exceptionally sensitive to tiny pose errors, meaning that even with posegraph optimization, a higher level of geometric alignment is required than what is typical for traditional trajectory correction. Second, the nature of LiDAR data leads to new representation issues. In unobserved regions such as the sky, or for distant objects where points are sparse, Gaussians can become distorted or grow uncontrollably, potentially leading to improper optimization of occluded Gaussians. This severely degrades the accuracy and realism of the final map.

To address these challenges, this paper proposes GS-Fusion, a novel LiDAR-Inertial-Visual SLAM system designed to effectively integrate LiDAR with 3DGS. To tackle the high-precision alignment requirement, we incorporate a surfel-to-surfel consistency constraint into our pose-graph optimization, which precisely aligns new observations with the existing map structure. For an efficient representation for distant objects, we introduce a pixel-aware initialization strategy that determines a Gaussian's scale based on its projected footprint in pixel space, rather than by Euclidean distance. Finally, to suppress geometric distortions in unobserved areas like the sky, we apply a bounded sigmoid function to constrain the maximum scale of the Gaussians.

The main contributions of this work are:

- An online LiDAR-Inertial-Visual Mapping system that tightly couples 3D Gaussian Splatting with surfel bundle adjustment.
- A pixel-aware Gaussian initialization strategy that reduces redundant splats and improves rendering quality.
- A bounded scale constraint to suppress excessive Gaussian growth in unobserved regions.
- A surfel-to-surfel consistency term for robust and globally consistent photorealistic using 3D Gaussians.

#### II. RELATED WORK

## A. Offline 3DGS with Pre-computed Poses

The seminal 3DGS paper [1] established an offline paradigm that first computes camera poses using a Structure-from-Motion (SfM) pipeline, such as COLMAP [2], before

Jaeseok Park and Chanoh Park are with the RovifyLab E-mails: jaeseok.park, chanoh.park@rovifylab.com

<sup>&</sup>lt;sup>2</sup> Jaeseok Park, Minsu Kim and Soohwan Kim are with Kwangwoon University, Seoul, Republic of Korea. E-mails: jaeseok.park, minsukim, kimsoohwan@kwu.ac.kr

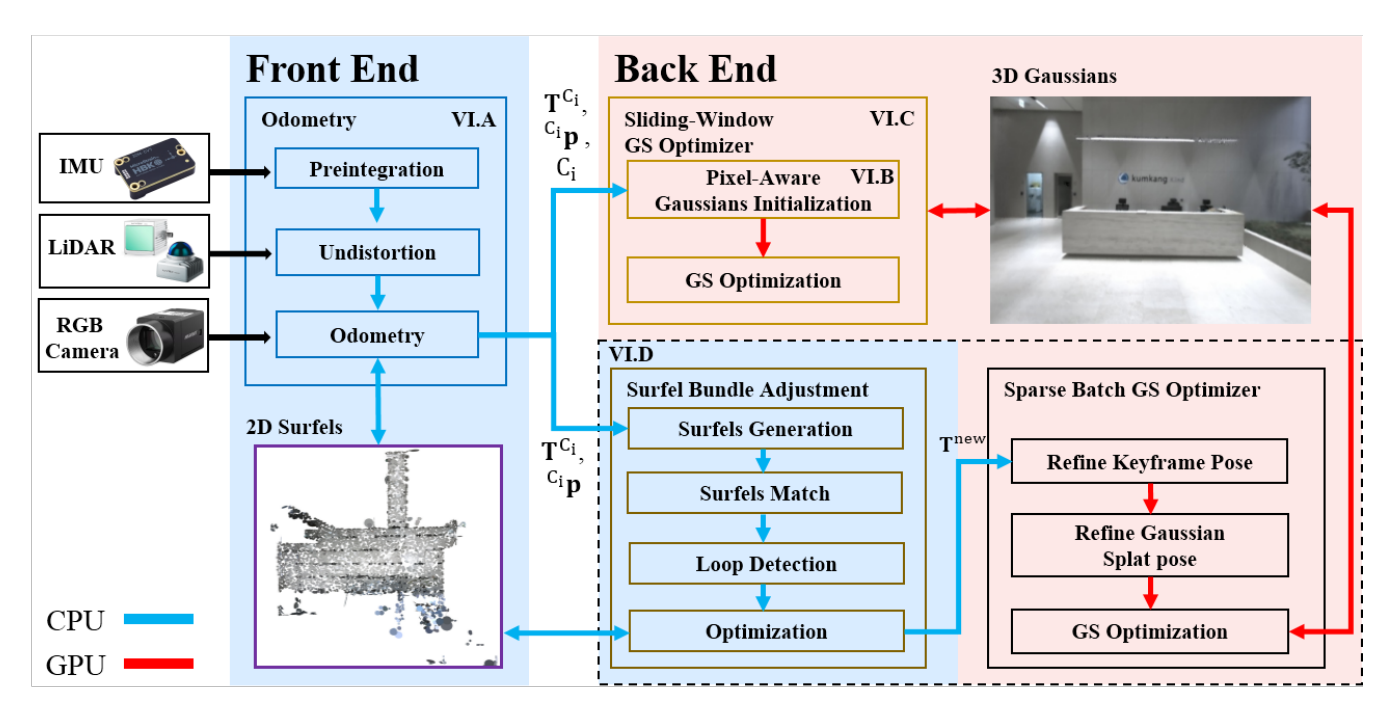


Fig. 1: **GSFusion System Overview** Dual-map architecture fuses LiDAR, camera, and IMU streams, tracking poses on a 2D surfel map while optimizing a pixel-aware 3D Gaussian map for photorealistic rendering. Loop closure then performs global refinement that jointly optimizes poses and Gaussians, yielding a geometrically consistent, high-resolution map.

optimizing the scene representation. This paradigm was extended by other work like GS-SDF [3], which sought to improve geometric accuracy with LiDAR regularization, and LetsGo [4], which utilized LiDAR trajectories for large-scale scenes. However, whether the poses are derived from SfM or even from advanced LiDAR-Inertial odometry systems such as LVI-SAM [5] and FAST-LIVO2 [6], the core problem remains: the map generation is a separate offline step. This fundamental division of pose estimation and rendering means that any sub-pixel pose errors are permanently "baked into" the system before optimization begins. This process inevitably propagates errors into the final map, creating "ghosting" artifacts and making realtime operation for robotics impossible. The limitations of this paradigm motivated the development of online systems that tightly couple localization and mapping.

## B. Online Visual-centric 3DGS

Subsequent online systems were primarily based on visual SLAM, but their reliance on visual information introduced critical vulnerabilities, such as sensitivity to environmental conditions. For instance, GS-ICP-SLAM [7] relies on a photometric ICP approach, making them prone to tracking failure in texture-poor regions, while Photo-SLAM [8] uses feature-based tracking that can struggle under abrupt motion or significant lighting changes. Although RGB-D sensors were introduced in SplaTAM [9] to regularize geometry, their short operational range and poor performance in strong sunlight confine them to smaller indoor scenes. Without geometric constraints, these vision-dependent systems can also suffer from uncontrolled Gaussian growth in regions

lacking points like the sky. This occurs because oversized Gaussians can occlude those behind them, hindering proper optimization and leading to degraded rendering quality. To solve this specific problem, we introduce a bounded scale constraint to limit the maximum size of Gaussians.

## C. Online LiDAR-Inertial-Visual 3DGS

The latest research has focused on combining the robustness of LiDAR with the photorealism of 3DGS, leveraging LiDAR's resilience to challenging lighting and textures as well as its precise long-range depth measurements. However, early hybrid approaches such as Gaussian-LIC [10] retained a vision-centric core that led to drift and rendering artifacts. More recent methods like LI-GS [11] and HGS-Mapping [11] have successfully fused the sensors but still leave two key challenges for photorealism unaddressed.

The first issue is global alignment. These systems rely on sparse pose-graph optimization, which aligns sensor trajectory at the keyframe level but lacks the dense, surface-level constraints needed for photorealism. The residual subpixel misalignments between the dense Gaussian map and the sparse pose graph, seen inc Gaussian-LIC, degrade rendering quality. To address this, we introduce a denser surfel-to-surfel consistency term to enforce a higher degree of geometric alignment.

Inefficient representation is the second challenge. These methods inherit the standard kNN-based initialization from the original 3DGS, which is ill-suited for the non-uniform density of LiDAR data. For sparse, distant points, this strategy creates an excessive number of ill-shaped Gaussians, bloating memory consumption and slowing down rendering.

We address this issue with a pixel-aware initialization strategy that creates a more compact and accurate map.

## III. SYSTEM OVERVIEW

Our system is built on two different map representations: a sparse map for localization and a dense map for photorealistic rendering. Inspired by the mapping philosophy of Elastic LiDAR Fusion [12], [13], this division allows the sparse map to focus on lightweight localization, while the dense map enables photorealistic rendering through back-end optimization.

The system's workflow, illustrated in Fig. 1, begins at the front-end, which processes synchronized LiDAR, camera, and IMU streams. Its primary role is real-time localization, achieved by tracking incoming LiDAR scans against the global sparse map provided by the back-end. Concurrently, it preprocesses data for the dense rendering map by initializing and locally refining 3D Gaussians. This processed information is then passed to the back-end, which maintains the two distinct global maps: a sparse, surfel-based geometric map for localization and the dense, 3D Gaussian map for photorealistic rendering. The back-end integrates new data into a pose graph, performs loop closure and global optimization, and updates both maps. Finally, the updated sparse map is fed back to the front-end, closing the loop and ensuring consistent, accurate tracking over time.

#### IV. METHODOLGY

In this section, we describe our LiDAR-Camera-IMU SLAM system, which combines surfel-based tracking, keyframe-based Surfel Bundle Adjustment(SBA), pixel-aware Gaussians initialization, and local-to-global photore-alistic mapping refinement.

## A. LiDAR-Inertial-Visual Odometry

We estimate the relative pose between consecutive keyframes by jointly optimizing geometric and photometric constraints, incorporating an initial motion prior from IMU preintegration [14]. The process begins with propagating the system state (pose, velocity, and bias) from keyframe i to j using the preintegrated IMU measurements.

For the geometric constraint, we extract surfels from the LiDAR point cloud of each keyframe and establish correspondences across adjacent frames [15]. A point-to-plane ICP residual is then formulated for each matched surfel pair  $(\mathbf{p}_i, \mathbf{p}_j)$  with its corresponding surface normal  $\mathbf{n}_j$ :

$$e_{icp} = \mathbf{n}_{j}^{\top} (^{W} \mathbf{R}_{j}^{-1} (^{W} \mathbf{R}_{i} \mathbf{p}_{i} + ^{W} \mathbf{t}_{i} - ^{W} \mathbf{t}_{j}) - \mathbf{p}_{j})$$
 (1)

where  $(\mathbf{R}_i, \mathbf{t}_i)$  and  $(\mathbf{R}_j, \mathbf{t}_j)$  are the global poses of keyframes i and j.

In parallel, for the photometric constraint, we select sparse feature points from the image and track them across keyframes [16]. The photometric residual is defined by directly comparing pixel intensities:

$$e_{photo} = \mathbf{I}_i(\mathbf{u}) - \mathbf{I}_j(\pi(^i\mathbf{R}_j\mathbf{p}_j + ^W \mathbf{t}_i))$$
 (2)

$$\pi(\mathbf{p}) = \begin{bmatrix} f_x \frac{X}{Z} + c_x \\ f_y \frac{Z}{Z} + c_y \end{bmatrix}$$
 (3)

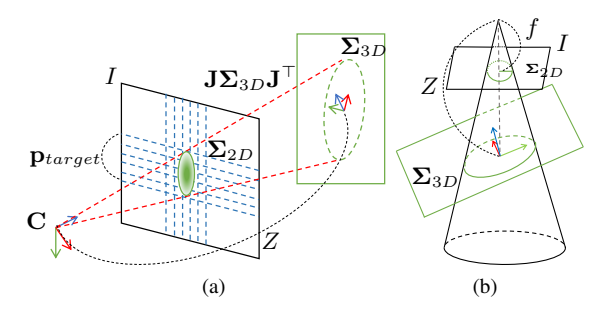


Fig. 2: **Pixel-Aware Gaussian Initialization** (a) illustrates the overall process of pixel-aware gaussian initialization, while (b) shows its relationship with conics

where  $\mathbf{I}_i(\mathbf{u})$  is the intensity of a pixel  $\mathbf{u}$  in frame i,  $\mathbf{p}_j$  is the 3D point corresponding to  $\mathbf{u}$ , and  ${}^i\mathbf{R}_j,{}^i\mathbf{t}_j$  is the relative transformation that transforms the point from frame j to frame i. The function  $\pi(\cdot)$  denotes the projection onto the image plane.

The full odometry cost function combines these two residuals:

$$L_{odom} = \sum \|e_{icp}\|^2 + \lambda \sum \|e_{photo}\|^2$$
 (4)

This cost is minimized to obtain a refined relative pose between keyframes, which serves as an odometry constraint in the global pose graph.

## B. Pixel-Aware Gaussian Initialization

Conventional LiDAR-based 3D Gaussian Splatting (3DGS) methods initialize Gaussian scales from local point density. This approach has a significant drawback: it creates overly large, blurry Gaussians in sparser, distant regions. To address this, our Pixel-Aware Gaussian Initialization strategy initializes 3D scales to ensure their projection onto the image plane maintains a consistent, predefined size, regardless of depth.

For each LiDAR point p, we first compute the local surface orientation via a K-Nearest Neighbors (KNN) search and Principal Component Analysis (PCA) to obtain a rotation matrix R. We then initialize the Gaussian as a flat ellipse aligned with the surface, setting anisotropic scales  $\sigma_x^2$  and  $\sigma_y^2$  in the tangent plane and scales  $\sigma_z^2$  along the normal. The 3D covariance matrix is thus defined as:

$$\Sigma_{3D} = \mathbf{R} \operatorname{diag}(\sigma_x^2, \sigma_y^2, \sigma_z^2) \mathbf{R}^{\top}$$
 (5)

To compute the projected covariance, we define the Jacobian  $\mathbf{J} \in \mathbb{R}^{2\times 3}$  of the camera projection function evaluated at  $\mathbf{p} = [X,Y,Z]^{\top}$ , assuming the pinhole camera model from Eq. (3):

$$\mathbf{J} = \begin{bmatrix} \frac{f_x}{Z} & 0 & -\frac{f_x X}{Z^2} \\ 0 & \frac{f_y}{Z} & -\frac{f_y Y}{Z^2} \end{bmatrix} \tag{6}$$

This Jacobian reflects how small perturbations in 3D space affect the projected position in the image. Notably, as the depth Z increases, the Jacobian entries decrease, resulting in smaller 2D projections Fig 2. This motivates the use of

**Algorithm 1:** Adaptive scaling adjustment of Gaussian splats. The upper threshold  $\sigma_{max}$  is increased when too many splats are saturated, and decreased when most are small, maintaining a balanced distribution of splat sizes.

Input: Current Gaussian scalings  $\{\mathbf{s}_{\text{old}}\}_{i=1}^{N}$ , current thresholds  $\sigma_{\max}$ ,  $\sigma_{\min}$ Output: Updated threshold  $\sigma_{\max}$ ,  $\mathbf{s}_{\text{new}}$ 1  $\max \sigma \leftarrow \{\|\text{BoundedSigmoid}(\mathbf{s}_{\text{old}}, \sigma_{\max})\|\}_{i=1}^{N}$ 2  $\operatorname{ratio_{top}} \leftarrow \frac{1}{N} \sum_{i=1}^{N} [\max \sigma_{i} > 0.95\sigma_{\max}]$ 3  $\operatorname{ratio_{low}} \leftarrow \frac{1}{N} \sum_{i=1}^{N} [\max \sigma_{i} < 0.05\sigma_{\max}]$ 4 if  $\operatorname{ratio_{top}} > 0.15$  then

5 |  $\operatorname{old} \leftarrow \sigma_{\max}$ 6 |  $\mathbf{s}_{\text{new}} \leftarrow \operatorname{BoundedSigmoid}(\mathbf{s}_{\text{old}}, \sigma_{\max})$   $\sigma_{\max} \leftarrow 1.2 \cdot \sigma_{\max}$ 7 else if  $\operatorname{ratio_{low}} > 0.95$  then

8 |  $\operatorname{old} \leftarrow \sigma_{\max}$ 9 |  $\mathbf{s}_{\text{new}} \leftarrow \operatorname{InverseBoundedSigmoid}(\mathbf{s}_{\text{old}}, \sigma_{\max})$   $\sigma_{\max} \leftarrow \operatorname{InverseBoundedSigmoid}(\mathbf{s}_{\text{old}}, \sigma_{\max})$   $\sigma_{\max} \leftarrow \operatorname{InverseBoundedSigmoid}(\mathbf{s}_{\text{old}}, \sigma_{\max})$   $\sigma_{\max} \leftarrow \operatorname{max}(0.8 \cdot \sigma_{\max}, 4 \cdot \sigma_{\min})$ 

conic-based scale adaptation to maintain consistent visibility. The 2D covariance of the projected Gaussian is then:

$$\mathbf{\Sigma}_{2D} = \mathbf{J}\mathbf{\Sigma}_{3D}\mathbf{J}^{\top} \tag{7}$$

We compute a scaling factor k as the ratio of the target radius  $r_{target}$  to the effective radius  $r_{eff}$  and apply it directly to the initial 3D scales to obtain the new, adapted scales  $\sigma'_x$ ,  $\sigma'_y$  and  $\sigma'_z$ :

$$r_{eff} = \sqrt[4]{\det(\mathbf{\Sigma}_{2D})}, \ k = \frac{r_{target}}{r_{eff}}$$
 (8)

$$\sigma'_x = k \cdot \sigma_x, \quad \sigma'_y = k \cdot \sigma_y, \quad \sigma'_z = k \cdot \sigma_z$$
 (9)

This initialization strategy produces flat, surface-aligned Gaussians with adaptive in-plane size, enabling efficient and stable rendering across varying depths and viewpoints.

## C. Local GS Mapping

While the initially assigned parameters of each Gaussian capture the rough structure of the environment based on LiDAR data, further refinement is required to achieve precise alignment and photorealistic rendering. As illustrated in Fig. 3, we refine the map by optimising the parameters of visible Gaussians within a fixed-size sliding window  $W = \{I_{i-K+1}, \ldots, I_i\}$  that contains the most recent K keyframes.

The rendered pixel  $\hat{I}(u,v)$  is computed using an alpha compositing equation that accumulates view-dependent colors weighted by opacity [1]:

$$\hat{I}(u,v) = \sum_{g} T_g \cdot \alpha_g \cdot C_g(\mathbf{v}_g), \quad T_g = \prod_{k=1}^{g-1} (1 - \alpha_k) \quad (10)$$

where Gaussians are sorted in front-to-back order based on their projected depth.

To quantify the discrepancy between the rendered image and the observed image I(u,v), we define a rendering loss

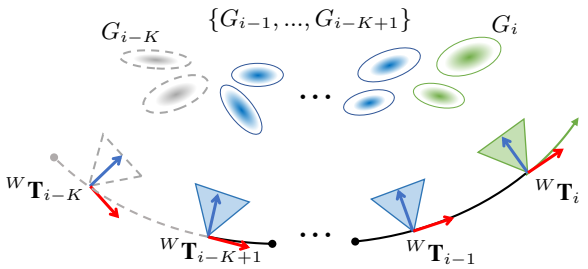


Fig. 3: **Sliding-window 3DGS Optimization.** At index i, we jointly optimize the most recent K camera keyframes  $\{\mathbf{T}_{i-K+1},\ldots,\mathbf{T}_i\}$  together with all Gaussians visible from them.

that combines an L1 difference with the Structural Similarity Index (SSIM) [17]:

$$L_{\text{render}} = (1 - \lambda_{\text{ssim}})L_{\text{L}1} + \lambda_{\text{ssim}}L_{\text{D-SSIM}}$$
 (11)

In regions with insufficient observations such as sky or background gaussians tend to grow excessively large during optimization. To prevent this, we apply a bounded sigmoid regularization on the learnable scale parameters s, ensuring that each gaussians extent remains within a defined range  $[\sigma_{\min}, \sigma_{\max}]$ :

$$\sigma_{\text{bounded}} = \sigma_{\min} + (\sigma_{\max} - \sigma_{\min}) \cdot \text{sigmoid}(s)$$
 (12)

The inverse mapping is given by:

$$s = \operatorname{sigmoid}^{-1} \left( \frac{\sigma_{\text{bounded}} - \sigma_{\min}}{\sigma_{\max} - \sigma_{\text{bounded}}} \right)$$
 (13)

While using a fixed upper bound  $\sigma_{max}$  is effective, we further improve stability by dynamically adjusting it based on the current distribution of Gaussian sizes. This adaptive process is detailed in Algorithm 1, where the BoundedSigmoid and InverseBoundedSigmoid functions correspond to Eq. (12) and Eq. (13), respectively.

For high-quality scene reconstruction, we employ a sequential optimization strategy. This process is divided into two distinct steps. First, in the local pose optimization stage, we refine the current camera poses  $\{\mathbf{T}_{i-K+1},...,\mathbf{T}_i\}$  by minimizing the geometric loss  $e_{\text{icp}}$ . Subsequently, with the pose held fixed, the gaussian refinement stage optimizes the parameters of visible gaussians by minimizing the photometric rendering loss  $L_{\text{render}}$ .

This entire two-step optimization process is performed within a sliding window framework to ensure real-time performance. When a new pose  $\mathbf{T}_{i+1}$  is added, the window slides forward by marginalizing the oldest pose  $\mathbf{T}_{i-K}$  and its associated Gaussians to maintain a fixed problem size. This approach efficiently decouples pose estimation from map refinement, leading to robust trajectory estimation and continuously improving rendering quality.

## D. Global GS Mapping

While local mapping improves geometric alignment and photorealistic rendering within short temporal windows, it does not explicitly address long-term drift or inconsistencies Algorithm 2: Surfel Bundle Adjustment Keyframe Refinement. Periodically retrieves optimized global keyframe trajectory  $\hat{\mathbf{T}}^{kf}$  from the SBA. If loop closure is detected, a sparse map refinement process is triggered. Missing poses are added

```
Input: Local Keyframe Trajectory T<sup>kf</sup>
    Output: Refined Global Trajectory \hat{\mathbf{T}}^{kf}
 1 optimized, loop \leftarrow GetTrajectory(\mathbf{T}^{kf})
 2 if optimized then
           \begin{array}{c|c} \textbf{for each} \ \mathbf{T}_i^{kf} \in \mathbf{T}^{kf} \ not \ in \ \hat{\mathbf{T}}_i^{kf} \ \textbf{do} \\ & \hat{T}_i^{kf} \leftarrow \hat{T}_{i-1}^{kf} \cdot \left(T_{i-1}^{kf}\right)^{-1} T_i^{kf} \end{array}
 3
 4
 5
            Apply trajectory refinement using \hat{T}^{kf}
 6
           if loop closure detected then
 7
                                     Trigger sparse map refinement
 8
           end
 9
10 end
```

that arise during large-scale exploration. To mitigate these issues, we perform global optimization over the full trajectory using a pose-graph framework that incorporates both motion and geometric constraints.

Each keyframe in the SLAM trajectory is represented as a node in the global pose graph, and two types of edges connect them, which are relative odometry constraints derived from the local frontend and surfel-to-surfel geometric alignments between spatially or temporally distant keyframes. The former ensures continuity, while the latter introduces long-range structure-preserving terms [12], [13].

The surfel-based alignment error between two keyframes i and j is formulated using the G-ICP [18] between corresponding surfels:

$$e_{\text{surfel}}(i,j) = \mathbf{d}^{\top} \left( \mathbf{\Sigma}_{j} + {}^{i} \mathbf{R}_{j} \mathbf{\Sigma}_{i}{}^{i} \mathbf{R}_{j}^{\top} \right)^{-1} \mathbf{d}$$
 (14)

$$\mathbf{d} = {}^{i}\mathbf{R}_{j}\mathbf{p}_{j} + {}^{i}\mathbf{t}_{j} - \mathbf{p}_{j} \tag{15}$$

where  $\Sigma_i$  and  $\Sigma_j$  are the covariance of matched surfels, and d is the error vector.

Global optimization minimizes the sum of both relative pose errors and surfel-based residuals over all pairs of connected keyframes:

$$L_{\text{global}} = \sum_{i,j} \|e_{\text{pose}}(i,j)\|^2 + \lambda_{\text{surfel}} \sum_{i,j} \|e_{\text{surfel}}(i,j)\|^2 \quad (16)$$

where  $e_{\rm pose}(i,j)$  is the relative pose constraint from odometry, and  $\lambda_{\rm surfel}$  is a weighting factor that balances geometric alignment with motion consistency.

To solve this optimization efficiently and incrementally, we employ iSAM2 [19], which updates only the affected parts of the pose graph without relinearizing the full system at every iteration. This allows our method to scale to long-term operations while maintaining computational efficiency.

After the global pose graph optimization converges, only a subset of keyframes  $\mathbf{T}^{\text{refined}}$  are typically affected. We update the Gaussians associated with these refined keyframes

to reflect their new poses. Specifically, for each keyframe  $\mathbf{T} \in \mathbf{T}^{\text{refined}}$ , we apply the following transformation to its associated Gaussians  $G^{\text{refined}}$ :

$$\forall \mathbf{G} \in G^{\text{refined}}: \quad \mathbf{p}_G^{\text{new}} = \mathbf{R}_{\mathbf{T}}^{\text{opt}} \mathbf{p}_G^{\text{old}} + \mathbf{t}_{\mathbf{T}}^{\text{opt}}$$
 (17)

$$\mathbf{R}_G^{\text{new}} = \mathbf{R}_T^{\text{opt}} \mathbf{R}_G^{\text{old}} \tag{18}$$

where  $\mathbf{p}_G^{\mathrm{old}}, \mathbf{R}_G^{\mathrm{old}}$  are the original Gaussian position and orientation, and  $\mathbf{R}_{\mathbf{T}}^{\mathrm{opt}}, \mathbf{t}_{\mathbf{T}}^{\mathrm{opt}}$  are the optimized keyframe pose.

Following this transformation, the spatial configuration of the Gaussians is aligned with the globally optimized keyframe trajectory. However, since these pose updates may introduce inconsistencies in appearance or surface coverage, we perform a second-stage refinement of the updated Gaussians to restore photorealistic rendering quality.

This refinement focuses solely on the internal parameters of the Gaussians such as scale, opacity, and spherical harmonics coefficients while keeping the camera poses fixed. We reuse the rendering loss function defined in Section IV.C, restricting its application to the updated Gaussian batch  $G^{\rm refined}$ :

$$L_{\text{render}}^{\text{refined}} = \sum_{\mathbf{T} \in \mathbf{T}^{\text{refined}}} L_{\text{render}}$$
 (19)

where  $L_{\rm render}^{\rm refined}$  denotes the rendering loss for a single keyframe, using the previously defined combination of L1 and SSIM terms.

This refinement is performed using the Adam optimizer and ensures that the appearance of the Gaussians remains consistent with observations, even after global pose adjustments. By limiting optimization to the affected regions, we preserve both visual fidelity and computational efficiency.

## V. EXPERIMENTS

We conducted experiments on desktop platform to evaluate the performance and deploy ability of the proposed system.

The main experiments, including comparative evaluations and ablation studies, were performed on a desktop equipped with an AMD Ryzen 9 7900 12-Core CPU, 64 GB RAM, and an NVIDIA RTX 4090 24 GB GPU. This environment allowed for the evaluation of the systems mapping consistency and runtime performance under unconstrained, high-throughput conditions.

## A. Experiments setup

To comprehensively evaluate the performance of our system, we conducted experiments on a combination of public and self-collected datasets covering both large-scale outdoor and small-scale indoor environments.

For the public datasets, we selected three sequences from the FAST-LIVO2 dataset [6] Retail\_Street, CBD02, and SYSU\_01 which represent diverse urban scenarios with varying levels of structural complexity. Additionally, we adopted two sequences from the MARS-LVIG dataset [20], namely HKairport01 and HKisland03. These UAV-based sequences include challenging terrain such as coastal and mountainous regions and are equipped with precisely calibrated sensor









Fig. 4: The experimental handheld deivce. The equipment used are the Livox AVIA (left) and the Livox MID-360 (right), each of which contains a 3D laser, an IMU, and a color camera.

data suitable for evaluating map consistency in complex environments.

To evaluate performance in structured indoor settings, we collected two custom datasets Reception and Demo room. These sequences were recorded in office-like and exhibition-style indoor environments. The constrained geometry and limited texture of these scenes allowed us to assess the robustness of our method in generating spatially consistent and stable maps.

For our custom datasets only, we performed additional calibration and synchronization to ensure accurate sensor alignment. Camera intrinsics and LiDAR-Camera extrinsics were estimated using the motion based calibration toolkit [21], which supports both pinhole and fisheye camera models. To achieve precise temporal alignment between all sensors, we employed the custom handheld device, which provides hardware-level time synchronization among LiDAR, camera, and IMU, as shown in Fig. 4 These steps ensured high-fidelity sensor fusion in the indoor experiments.

#### B. Rendering Comparison with Existing Methods

Table I contrasts our proposed GSFusion (Ours) with existing methods GS-SDF [3] (30k iterations), LetsGo [4] (15k iterations), Photo-SLAM [8], and GS-ICP-SLAM [7] in terms of reconstruction fidelity (PSNR), final map size (Mem.), and full-sequence processing time (Dur.).

As shown in Table I, our method demonstrates a superior balance between rendering quality and efficiency across the public datasets. For our method, we tested two variants of our pixel-aware initialization using 1 and 5 pixels, denoted as Ours(1pixel) and Ours(5pixel), respectively. Notably, our Ours(1pixel) variant achieves the highest PSNR scores on the CBD02, Retail, SYSU01, and airport03 datasets, outperforming the existing methods. The corresponding qualitative results, including rendered images and error maps, are presented in Fig. 5. The Ours(5pixel) variant significantly reduces the final map size with only a slight decrease in PSNR, achieving the smallest map on most datasets (e.g., 24.7MB on SYSU01 and 31.0MB on Retail). Thus, our method delivers high-fidelity results without the significant optimization time and storage demands of competing approaches such as GS-SDF and LetsGo.

Even in cases where Photo-SLAM reports a higher PSNR, such as on the island01 dataset, our system provides a competitive alternative with far fewer resources. For instance, on

TABLE I: Rendering Comparison with Existing Methods

Dataset	Method	PSNR↑	Map(MB)↓	Dur.(sec)↓					
Open Datasets									
	GS-SDF	17.4	287.1	589					
CBD02	LetsGo	24.3	203.0	516					
	Photo-SLAM	20.2	171.7	319					
	GS-ICP-SLAM	18.1	288.3	321					
	Ours(1pixel)	27.5	235.0	296					
	Ours(5pixel)	27.0	55.2	296					
Retail	GS-SDF	27.2	451.1	1032					
	LetsGo	29.0	293.2	343					
	Photo-SLAM	28.3	84.6	153					
	GS-ICP-SLAM	18.7	74.3	147					
	Ours(1pixel)	29.2	111.7	145					
	Ours(5pixel)	28.1	31.0	145					
SYSU01	GS-SDF	16.5	308.0	1752					
	LetsGo	26.7	307.5	486					
	Photo-SLAM	23.6	81.3	193					
	GS-ICP-SLAM	18.3	275.2	399					
	Ours(1pixel)	27.8	90.2	183					
	Ours(5pixel)	27.9	24.7	183					
airport03	GS-SDF	_	-	-					
	LetsGo	17.3	329.1	843					
	Photo-SLAM	16.9	77.9	265					
1	GS-ICP-SLAM	_	_	-					
	Ours(1pixel)	20.0	146.4	334					
	Ours(5pixel)	19.7	47.1	334					
	GS-SDF	-	_	-					
	LetsGo	16.7	428.0	1664					
island01	Photo-SLAM	21.1	31.2	210					
	GS-ICP-SLAM	-	-	-					
	Ours(1pixel)	18.6	74.79	653					
	Ours(5pixel)	18.6	38.1	653					
	Ours	s Datasets							
	GS-SDF	28.1	199.9	952					
Demo room	LetsGo	25.4	107.7	277					
	Photo-SLAM	28.1	17.2	170					
	GS-ICP-SLAM	22.9	87.0	46					
	Ours(1pixel)	25.5	166.5	142					
	Ours(5pixel)	28.3	57.5	142					
	GS-SDF	26.2	314.1	1427					
Reception	LetsGo	27.7	31.5	209					
	Photo-SLAM	22.6	31.4	117					
	GS-ICP-SLAM	22.7	181.6	174					
	Ours(1pixel)	23.4	94.8	96					
	Ours(5pixel)	26.7	26.8	96					

*Note:* - denotes that the baseline method either failed or its results were not available on the given dataset.

island01, our Ours(5pixel) method achieves a higher PSNR than LetsGo (18.6 vs. 16.7) with a map size over 10 times smaller (38.1 MB vs. 428.0 MB). On our in-house Reception and Demo Room datasets, our method recorded the fastest processing time (96 seconds), and the Ours(5pixel) version produced the smallest map (26.8 MB) while delivering a PSNR close to the top performer. This clearly highlights its key advantages for resource-constrained applications.

Overall, our pixel-aware approach provides the best tradeoff between reconstruction quality, efficiency, and practical deploy ability. Across all public datasets, our system produces results with PSNR nearly on par with the bestperforming baselines while requiring only a fraction of the map storage and computational time.

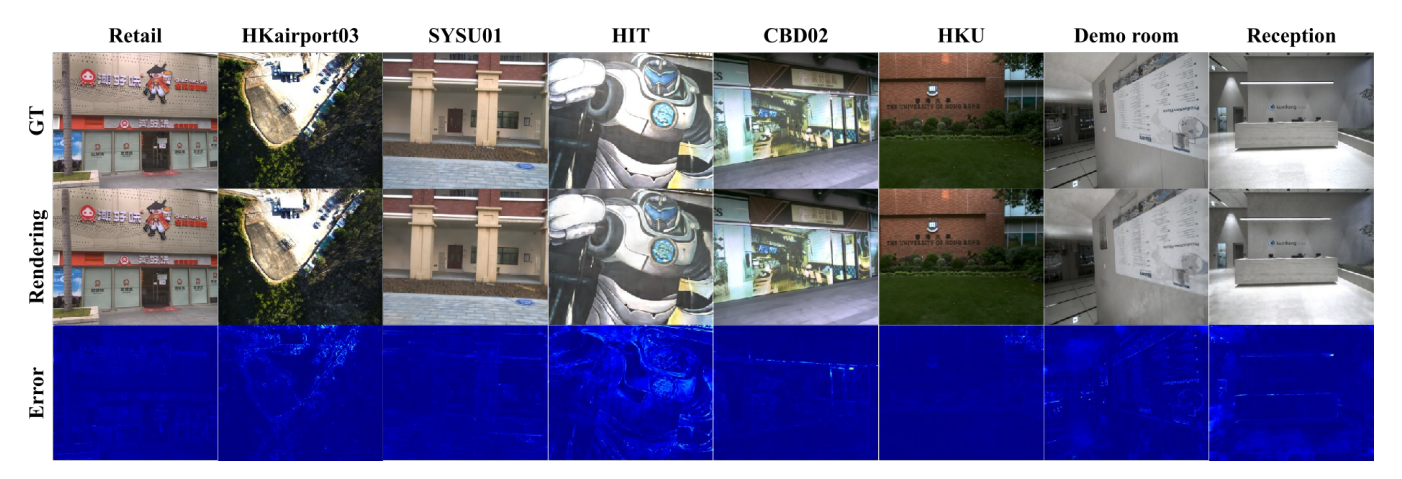


Fig. 5: Qualitative rendering results of our proposed GSFusion system. Each column represents a dataset, with rows displaying the Ground Truth (GT), our rendered image and the error map.



Fig. 6: **Render results of the ablation study.** Subfigure (a) shows the result without our surfel-to-surfel consistency term, while (b) shows the result with it applied. Similarly, (c) shows the output without the bounded sigmoid constraint, which is included in (d).

TABLE II: Ablation study

D	3.5	BS(x)	BS(x)	BS(O)	BS(O)
Dataset	Metric	SBA(x)	SBA(O)	SBA(x)	SBA(O)
CBD02	PSNR↑	26.9	27.4	27.0	27.7
	$\max\sigma\downarrow$	690.23	599.54	0.43	0.43
	Dur.(sec)↓	245	245	245	245
Retail	PSNR↑	28.0	28.2	28.3	28.5
	$\max\sigma\downarrow$	71.29	59.04	0.34	0.34
	Dur.(sec)↓	145	145	145	145
Desk	PSNR↑	27.0	27.2	24.5	26.7
	$\max\sigma\downarrow$	105.17	154.07	0.12	0.11
	Dur.(sec)↓	96	96	96	96

Note: BS denotes the Bounded Sigmoid, and SBA denotes the Surfel Bundle Adjustment.

## C. Surfel Bundle Adjustment

Surfel Bundle Adjustment(SBA) effectively improves the global consistency of camera poses. After optimization, the relative alignment of keyframes becomes more stable, and large-scale drift is significantly suppressed. However, because surfel bundle adjustment does not modify the scale or shape of Gaussians, excessively large splats persist in the map. As shown in Table II, while PSNR improves modestly across all sequences (e.g., from 26.9 dB to 27.4 dB on CBD02), the maximum Gaussian scale remains large-up to 0.6 meters-leading to visual and geometric artifacts.

This issue is particularly evident when the map is viewed from a free view perspective. Due to their oversized scale, individual Gaussians tend to overlap and merge, blurring object boundaries and corrupting the structural integrity of the scene. As illustrated in Fig. 6,(a) and (b), straight walls appear curved or smeared, and fine-scale geometry is lost under the spread of neighboring splats. In extreme cases, the Gaussian footprint becomes so large that it spans multiple objects, erasing the spatial distinction between them.

Such distortion degrades not only visual clarity but also the geometric reliability of the map, which is critical for downstream applications such as path planning, semantic labeling, and 3D reconstruction. While SBA boosts PSNR by refining alignment, as shown in Table II, it does not prevent the underlying scale-induced geometric collapse. This observation motivates the need for explicit scale control, such as the bounded sigmoid constraint, to ensure that each Gaussian remains spatially compact and faithfully represents the underlying structure of the scene.

## D. Bounded Sigmoid Impact on Geometry consistency

While surfel bundle adjustment improves camera alignment, it does not resolve the geometric distortion caused by oversized Gaussians. To address this, we apply a bounded sigmoid constraint that explicitly limits Gaussian scale during training [22]. As shown in Table II, this constraint

reduces the maximum scale from 690 m to 0.43 m on CBD02, and similarly across Retail (71 m  $\rightarrow$  0.34 m) and Desk (105 m  $\rightarrow$  0.11 m), with no change in runtime.

This scale control greatly improves map geometry. The visual improvement, where divergence is suppressed, is clearly demonstrated by comparing Fig. 6,(c) and (d). Large, overlapping splats are suppressed, and the reconstructed structures better match the true layout, especially in top-down views. Although PSNR slightly drops on Reception  $(27.0\,\mathrm{dB} \to 24.5\,\mathrm{dB})$  due to reduced smoothing in sparse regions, it improves on Retail  $(28.0\,\mathrm{dB} \to 28.3\,\mathrm{dB})$  and remains stable on CBD02.

When combined with SBA, the system achieves the best overall result, where PSNR reaches 28.5 dB, geometry is preserved, and performance remains real-time. This confirms that the bounded sigmoid constraint is essential for preventing scale-induced artifacts and maintaining structural fidelity throughout the map.

## VI. CONCLUSION

We presented GSFusion, a real-time LiDAR-IMU-Camera SLAM system that integrates 3D Gaussian Splatting with surfel-based trajectory optimization to achieve photorealistic mapping with real-time performance. By introducing a pixel-aware gaussian initialization strategy and a bounded sigmoid constraint, our system reduces redundant splats and maintains stable rendering quality, even in sparsely observed regions. Experiments on public and custom datasets demonstrate improved rendering quality and memory efficiency compared to prior 3DGS-based SLAM approaches, highlighting how the integration of our proposed components enables scalable and practical SLAM in real-world scenarios.

Future work will address current limitations, such as handling dynamic scenes and reflections, by incorporating dynamic modeling and learning-based appearance components. Furthermore, we will explore mechanisms for global map updates to mitigate issues from inaccurate loop closures and improve long-term consistency.

## REFERENCES

- [1] B. Kerbl, G. Kopanas, T. Leimkuehler, and G. Drettakis, "3D Gaussian Splatting for Real-Time Radiance Field Rendering," *ACM Trans. Graph.*, vol. 42, no. 4, pp. 139:1–139:14, 2023.
- [2] J. L. Schonberger and J.-M. Frahm, "Structure-from-Motion Revisited," in 2016 IEEE Conference on Computer Vision and Pattern Recognition (CVPR). Las Vegas, NV, USA: IEEE, June 2016, pp. 4104–4113.
- [3] J. Liu, Y. Wan, B. Wang, C. Zheng, J. Lin, and F. Zhang, "GS-SDF: LiDAR-Augmented Gaussian Splatting and Neural SDF for Geometrically Consistent Rendering and Reconstruction," http://arxiv.org/abs/2503.10170, Mar. 2025.
- [4] J. Cui, J. Cao, F. Zhao, Z. He, Y. Chen, Y. Zhong, L. Xu, Y. Shi, Y. Zhang, and J. Yu, "LetsGo: Large-Scale Garage Modeling and Rendering via LiDAR-Assisted Gaussian Primitives," ACM Trans. Graph., vol. 43, no. 6, pp. 172:1–172:18, 2024.
- [5] T. Shan, B. Englot, C. Ratti, and D. Rus, "LVI-SAM: Tightly-coupled Lidar-Visual-Inertial Odometry via Smoothing and Mapping," in 2021 IEEE International Conference on Robotics and Automation (ICRA). Xi&anos:an China: IEEE Press 2021, pp. 5692–5698
- Xi'an, China: IEEE Press, 2021, pp. 5692–5698.
  [6] C. Zheng, W. Xu, Z. Zou, T. Hua, C. Yuan, D. He, B. Zhou, Z. Liu, J. Lin, F. Zhu, Y. Ren, R. Wang, F. Meng, and F. Zhang, "FAST-LIVO2: Fast, Direct LiDAR-Inertial-Visual Odometry," *IEEE Transactions on Robotics*, vol. 41, pp. 326–346, 2025.

- [7] S. Ha, J. Yeon, and H. Yu, "RGBD GS-ICP SLAM," in Computer Vision ECCV 2024: 18th European Conference, Milan, Italy, September 29–October 4, 2024, Proceedings, Part XXXVI. Berlin, Heidelberg: Springer-Verlag, 2024, pp. 180–197.
- [8] H. Huang, L. Li, H. Cheng, and S.-K. Yeung, "Photo-SLAM: Real-Time Simultaneous Localization and Photorealistic Mapping for Monocular, Stereo, and RGB-D Cameras," in 2024 IEEE/CVF Conference on Computer Vision and Pattern Recognition (CVPR), June 2024, pp. 21584–21593.
- [9] N. Keetha, J. Karhade, K. M. Jatavallabhula, G. Yang, S. Scherer, D. Ramanan, and J. Luiten, "SplaTAM: Splat, Track & Map 3D Gaussians for Dense RGB-D SLAM," in 2024 IEEE/CVF Conference on Computer Vision and Pattern Recognition (CVPR), June 2024, pp. 21 357–21 366.
- [10] X. Lang, L. Li, C. Wu, C. Zhao, L. Liu, Y. Liu, J. Lv, and X. Zuo, "Gaussian-LIC: Real-Time Photo-Realistic SLAM with Gaussian Splatting and LiDAR-Inertial-Camera Fusion," http://arxiv.org/abs/2404.06926, Sept. 2024.
- [11] C. Jiang, R. Gao, K. Shao, Y. Wang, R. Xiong, and Y. Zhang, "LI-GS: Gaussian Splatting With LiDAR Incorporated for Accurate Large-Scale Reconstruction," *IEEE Robotics and Automation Letters*, vol. 10, no. 2, pp. 1864–1871, Feb. 2025.
- [12] C. Park, P. Moghadam, S. Kim, A. Elfes, C. Fookes, and S. Sridharan, "Elastic LiDAR Fusion: Dense Map-Centric Continuous-Time SLAM," in 2018 IEEE International Conference on Robotics and Automation (ICRA), May 2018, pp. 1206–1213.
- [13] C. Park, P. Moghadam, J. L. Williams, S. Kim, S. Sridharan, and C. Fookes, "Elasticity Meets Continuous-Time: Map-Centric Dense 3D LiDAR SLAM," *IEEE Transactions on Robotics*, vol. 38, no. 2, pp. 978–997, Apr. 2022.
- [14] C. Forster, L. Carlone, F. Dellaert, and D. Scaramuzza, "On-Manifold Preintegration for Real-Time Visual-Inertial Odometry," *IEEE Transactions on Robotics*, vol. 33, no. 1, pp. 1–21, Feb. 2017.
- [15] C. Park, S. Kim, P. Moghadam, C. Fookes, and S. Sridharan, "Probabilistic Surfel Fusion for Dense LiDAR Mapping," in 2017 IEEE International Conference on Computer Vision Workshops (ICCVW), Oct. 2017, pp. 2418–2426.
- [16] C. Forster, M. Pizzoli, and D. Scaramuzza, "SVO: Fast semi-direct monocular visual odometry," in 2014 IEEE International Conference on Robotics and Automation (ICRA), May 2014, pp. 15–22.
- [17] Z. Wang, A. Bovik, H. Sheikh, and E. Simoncelli, "Image quality assessment: From error visibility to structural similarity," *IEEE Trans*actions on Image Processing, vol. 13, no. 4, pp. 600–612, Apr. 2004.
- [18] A. Segal, D. Haehnel, and S. Thrun, "Generalized-ICP," in *Robotics: Science and Systems V*. Robotics: Science and Systems Foundation, June 2009.
- [19] M. Kaess, H. Johannsson, R. Roberts, V. Ila, J. J. Leonard, and F. Dellaert, "iSAM2: Incremental smoothing and mapping using the Bayes tree," *International Journal of Robotics Research*, vol. 31, no. 2, pp. 216–235, 2012.
- [20] H. Li, Y. Zou, N. Chen, J. Lin, X. Liu, W. Xu, C. Zheng, R. Li, D. He, F. Kong, Y. Cai, Z. Liu, S. Zhou, K. Xue, and F. Zhang, "MARS-LVIG dataset: A multi-sensor aerial robots SLAM dataset for LiDAR-visual-inertial-GNSS fusion," *International Journal of Robotics Research*, vol. 43, no. 8, pp. 1114–1127, 2024.
- [21] C. Park, P. Moghadam, S. Kim, S. Sridharan, and C. Fookes, "Spatiotemporal Camera-LiDAR Calibration: A Targetless and Structureless Approach," *IEEE Robotics and Automation Letters*, vol. 5, no. 2, pp. 1556–1563, Apr. 2020.
- [22] J. T. Barron, B. Mildenhall, D. Verbin, P. P. Srinivasan, and P. Hedman, "Mip-NeRF 360: Unbounded Anti-Aliased Neural Radiance Fields," in 2022 IEEE/CVF Conference on Computer Vision and Pattern Recognition (CVPR), June 2022, pp. 5460–5469.